



# A dielectric horn antenna and lightweight radar system for material inspection

Jana Ježová\*, Sébastien Lambot

Université catholique de Louvain, Earth and Life Institute, Croix du Sud 2/L7.05.02, 1348 Louvain-la-Neuve, Belgium

## ARTICLE INFO

### Article history:

Received 12 September 2018

Received in revised form 3 June 2019

Accepted 12 July 2019

Available online 22 July 2019

### Keywords:

Dielectric TEM horn

Lightweight radar system

Non-invasive inspection

## ABSTRACT

In this paper, we set up a lightweight, frequency-domain radar system using a handheld vector network analyser combined with air-coupled and dielectric-coupled horn antennas. A new positioning system with a binary barcode ruler, reading webcam and an algorithm for its recognition was developed. The radar system was tested on several media using both the air-coupled and dielectric-coupled antennas, namely, on a laboratory model containing sand and on a concrete block with a metallic reinforcement. The resulting GPR images demonstrated the good functioning of the radar system. In our experiments, both antennas and the whole lightweight radar system provided radar images which permitted to clearly detect the buried objects. Furthermore, the dielectric-coupled horn antenna showed better coupling with the investigated materials, resulting in higher-quality radar images.

© 2019 Elsevier B.V. All rights reserved.

## 1. Introduction

Subsurface non-destructive inspection using ground-penetrating radar (GPR) is a discipline which is already very well described in many publications (Annan, 2002; Daniels, 2000; Casas et al., 2000). GPR is an efficient non-destructive device which was used in various different fields, such as civil and transport engineering (Alani and Tosti, 2018; Kilic and Eren, 2018; Benedetto et al., 2017), landmine detection (Savelyev et al., 2007; Sato et al., 2012), archaeology (Persico et al., 2014; Angelis et al., 2018; Liu et al., 2018), environmental applications (Hong et al., 2018; Jonard and Weihermã, 2012; Ardekani et al., 2016; André et al., 2012), and progressively also wooden samples (Reci et al., 2016; Rodríguez-Abad et al., 2010), tree roots (Nichols et al., 2017; Al Hagrey, 2007) and tree trunks investigations (Ježová et al., 2016; Weilin Li and Jian Wen, 2018). This technology is based on the scattering of electromagnetic waves radiated from a transmitting antenna into a medium where they are partially reflected from electromagnetic contrasts and subsequently recorded by a receiving antenna. The transmitter and receiver consist of a single antenna (monostatic radar system) or can consist of two or several antennas (bistatic or multistatic radar systems).

GPR operates with various kinds of antennas with specific designs to achieve a good range resolution. These conditions include large bandwidth, low side lobes and in the case of separate transmitting and receiving antennas, low cross-coupling levels (Grosvenor et al., 2007). Antennas applicable for impulse radar systems are, for example, spiral (Sato et al., 2005), Vivaldi (Sarkis & Craeye, 2010), bowtie (Congedo

et al., 2010), dipole (Qin and Xie, 2016), or transverse electromagnetic (TEM) horn (Mallahzadeh et al., 2008). The TEM horn has been widely used as a very proficient ultra-wideband antenna (Malherbe and Barnes, 2007; Qi et al., 2015). It is used for various applications, such as electromagnetic compatibility (EMC) experiments, GPR, Free-space Time-Domain (FTD) measurement systems, and feeds for reflectors (Ascama et al., 2013; Bird et al., 2013). This antenna is characterized by a large bandwidth, good directivity, no dispersion, and relatively easy construction (Karshenas et al., 2009). A conventional air-filled TEM horn antenna consists of a flared waveguide (metal plates, wires, etc.) (Kao et al., 2008). The tapering of the metal plates gradually changes in order to increase the impedance of the antenna usually from  $50 \Omega$  at the antenna feed to match with the coaxial cable up to  $377 \Omega$  at the aperture to match with air (or lower to match with other media) (Wiesbeck et al., 2009). The impedance variation within the antenna can be linear, Chebyshev, exponential, Hecken, etc. (Bassam and Rashed-Mohassel, 2006; Malherbe and Barnes, 2007). To improve coupling between antennas and coaxial cables, baluns are often used (Foster and Tun, 1995; Manteghi and Rahmat-Samli, 2004).

During data acquisition, it is important to keep good contact of the antenna with the surface to avoid large surface reflections caused by the difference between the electromagnetic properties of air and those from the inspected medium. This rule is crucial mainly for materials with relatively high dielectric constants (e.g., living wood with  $\epsilon_r > 10$ ). To achieve a good coupling between the antenna and the surface, a usage of similar materials is suggested. For instance, a dielectric-filled TEM horn antenna design can be used. Yarovoy et al. (2002) and Lestari et al. (2000) developed dielectric antennas to achieve good matching with sand in order to improve their landmine detection technique. They used media based on silicone with a relative permittivity  $\epsilon_r$

\* Corresponding author.

E-mail address: [jana.jezova@gmail.com](mailto:jana.jezova@gmail.com) (J. Ježová).

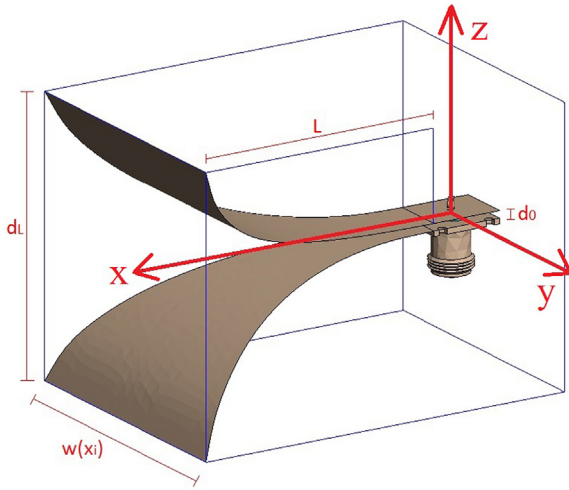


**Fig. 1.** General shape of the TEM horn antenna.  $d_0$  and  $d_L$  are distances between the waveguides at the antenna feed and aperture, respectively,  $w(x_i)$  is the waveguide width and  $L$  is the length of the antenna.

ranging from about 2.9 to 4. Khalaj Amineh et al. (2009) used the dielectric TEM horn antenna with a special cement (ECCOSTOCK HiK Cement) with  $\epsilon_r = 10$  for breast imaging to reach good coupling with a human body which is very humid, and thus, having a relatively high permittivity.

The objective of this research was to develop an ultra-wideband frequency domain antenna with a functional radar system, which is suitable for investigating objects such as walls, concrete or tree trunks. In that respect, two TEM horn antennas were developed and tested, namely, an air-coupled horn and a dielectric-coupled horn. The air-coupled antenna was designed according to the modified design suggested by Mallahzadeh and Karshenas (2009). Then, a dielectric-coupled antenna with a similar shape was suggested. Section 2 explains how we selected suitable dielectric for our antenna. To optimize the antenna and to see differences between its theoretical and real performance, it was simulated using FEKO (Altair Engineering Inc., Troy, Michigan, USA) software. In that matter, the 3D images of the total gain and the electric field in the  $E$ -plane were studied for both antennas. After manufacturing the antennas, they were calibrated and their free-space responses were compared with the simulated values. In order to have good ergonomics, we set up a lightweight radar system using both TEM horn antennas, a handheld vector network analyser (VNA), a microcomputer, an external battery, and a webcam for positioning. Furthermore, a special mobile application was developed in order to remotely control the radar system with a common smartphone, tablet or computer. The whole radar system was subsequently tested over a sandbox with a buried metal bar, on a laboratory cylindrical model filled with sand, and on a known concrete structure. The possibility of satisfactory data acquisition and ease of manipulation with the radar system were tested, discussed and evaluated.

## 2. Design of the horn antennas

### 2.1. Antenna geometry

Considering a very efficient performance, size and a relatively easy construction, a TEM horn appeared as a very convenient antenna for the lightweight radar system. In our previous experiments (Ježová et al., 2017), we used a custom-made air-coupled TEM horn antenna for the inspection of a cylindrical laboratory model and for the detection of a plastic pipe buried in a sandbox. This antenna was constructed according to a design suggested by Mallahzadeh and Karshenas (2009) for  $f_{min} = 1.0$  GHz. First of all, the linear trend of the impedance was

chosen due to its easier construction. The air-coupled antenna was designed using Eqs. (1) and (2) which describe the tapering (or widening)  $d(x_i)$  of the waveguides in direction  $x$  (see Fig. 1) (Mallahzadeh and Karshenas, 2009):

$$d(x_i) = a \cdot e^{b \cdot x_i} \quad (1)$$

$$a = d_0 \quad b = \frac{1}{L} \cdot \ln\left(\frac{d_L}{d_0}\right) \quad (2)$$

where  $d_0$  and  $d_L$  are distances between the waveguides at the feed and the aperture of the antenna, respectively, and  $L$  is the length of the antenna given by:

$$L = \lambda_{max} \cdot 4 \quad \lambda_{max} = \frac{c}{f_{min} \cdot \sqrt{\epsilon_r}} \quad (3)$$

where  $\lambda_{max}$  is the maximal wavelength [m],  $c$  is the speed of light in vacuum [m/s], and  $f_{min}$  is the lower cutoff frequency of the antenna. Eq. (4) describes the width  $w(x_i)$  of the metal plates (waveguides), in the  $y$  direction, as a function of  $x$ :

$$w(x_i) = \frac{d(x_i)}{Z(x_i)} \cdot \eta \quad (4)$$

where  $Z(x_i)$  is the characteristic impedance as a function of  $x$  and  $\eta$  is the free space impedance ( $120\pi \Omega$ ). The characteristic impedance  $Z(x_i)$  has a linear increase from 50 to  $120\pi \Omega$  to match with the 50  $\Omega$  connector at the antenna feed and the free space at the antenna aperture.

During our laboratory experiments, we aimed to work with dry sand as a filling material for our cylindrical model. Hence, to better couple the TEM horn antenna with the sand, we filled it with a material with similar properties. In that respect, several materials were tested as filling dielectrics (e.g., cement, dry sand). After several experiments, paraffin wax turned out to be the best trade-off between the dielectric loss, stability and availability of the material as its relative permittivity  $\epsilon_r = 2.2$  and its loss tangent  $\delta = 2 \cdot 10^{-4}$ . Furthermore, it was a very

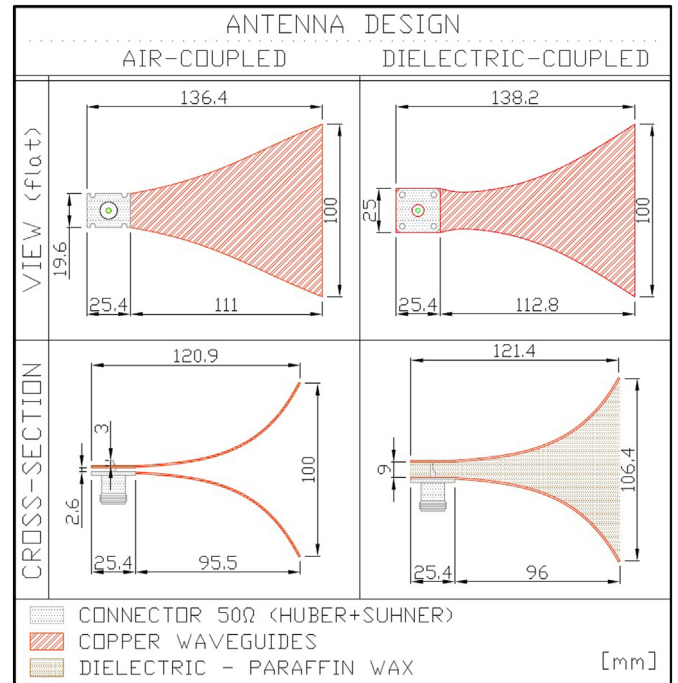


**Fig. 2.** Design of both antennas: a) air-coupled with  $f_{min} = 1$  GHz on the left, b) dielectric-coupled with  $f_{min} = 0.65$  GHz on the right. In the upper part, these are views on the flat antenna waveguides. In the lower part, these are cross-sections of the antennas with the curved waveguides.

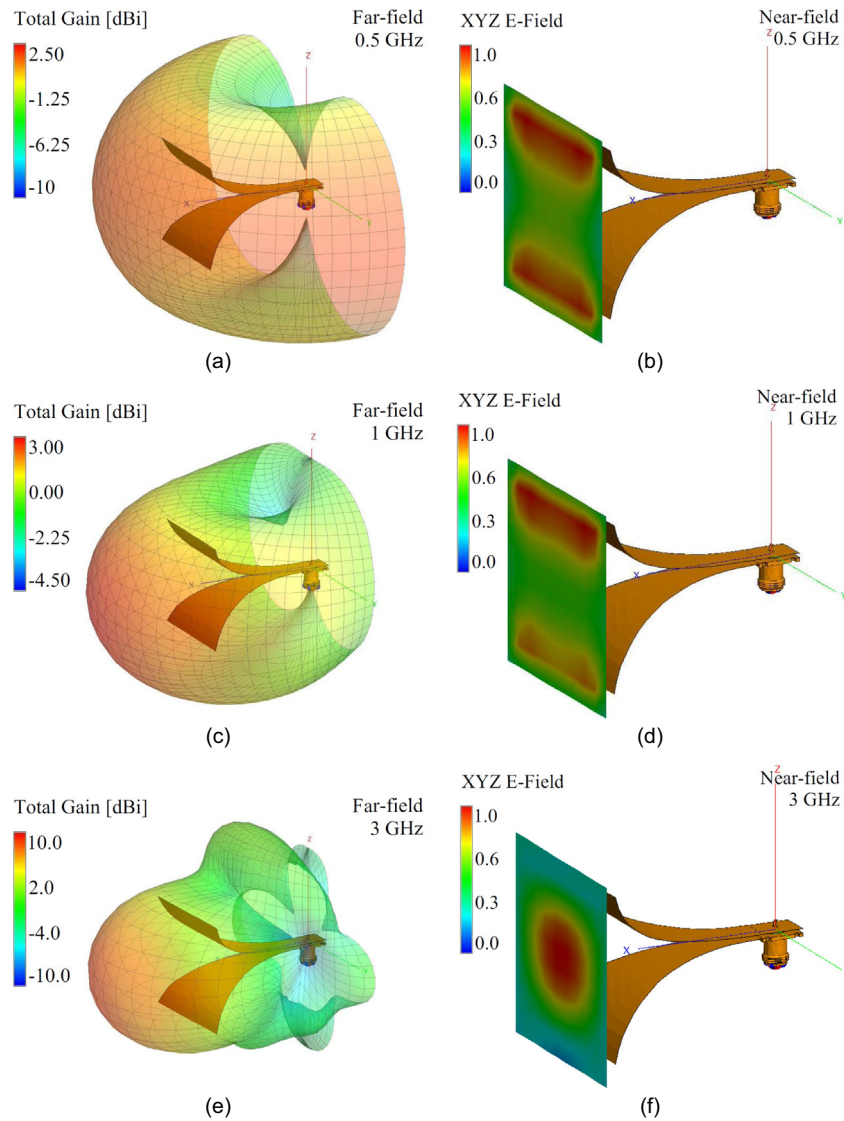


**Fig. 3.** Electromagnetic simulation using FEKO. Total gain in far-field [dBi] (on the left) and normalized electric field in E-plane (on the right) for the air-coupled antenna for three different frequencies (0.5, 1 and 3 GHz).

easy material to work with. The dielectric antenna was designed following the same equations as for the air-coupled antenna. Nevertheless, for the new geometry of the dielectric-coupled antenna, the characteristic impedance in the dielectric  $Z_d(x_i)$  had to be recalculated using Eq. (5). Furthermore, as the length of the antenna was kept, the minimum frequency  $f_{min}$  changed from about 1 GHz (for the air-coupled antenna) to about 0.65 GHz (for the dielectric-coupled antenna).

$$Z_d(x_i) = \frac{Z(x_i)}{\sqrt{\epsilon_r}} \quad (5)$$

where  $\epsilon_r$  is a relative permittivity of the filling material. The final shape of the antennas is displayed in Fig. 2, with the flat (before curving) waveguides view and the cross-section of the antenna (after curving).

The waveguides of the antennas were made of 1 mm thick copper plates. Copper is a material which is very easy to work with in terms of shaping (it is relatively flexible) and it has an excellent electrical conductivity ( $\approx 5.96 \cdot 10^7$  S/m). After the dielectric-coupled antenna waveguides assembling, a plastic cover was fixed around the antenna to follow the shape of the structure. Then, the paraffin wax was melted and filled into the antenna. When the wax was solid again, the plastic cover was removed. To observe the limiting abilities of the antennas,

they were tested in the frequency range of 0.5–3.5 GHz to overlap their minimum frequencies and see their operating range. This antenna was initially designed for the specific application of tree trunk imaging, and hence, this frequency range was chosen. Living wood is relatively humid, so even though it might have been possible to reach higher frequencies with the same size of the antenna, it would have been counterproductive due to relatively high attenuation.

## 2.2. Numerical simulations

In order to evaluate the theoretical performances of the antennas, the FEKO software was used. We analysed its isotropic gain and radiation pattern. The electric field in the E-plane was also analysed. Then, their return loss, referred to as  $H_i$  in this paper, was simulated and compared with the measured data. The total gain and the electric field in the E-plane for the air-coupled antenna is displayed in Fig. 3. Fig. 4 displays the same function for the dielectric-coupled antenna. We examined those parameters for three frequencies, namely, 0.5, 1 and 3 GHz. In the lower frequencies (0.5 GHz in this case), the radiation pattern is very similar for both antennas. The maximum gain reaches about 2.5 dBi and it is distributed following a doughnut shape which is not very typical for horn antennas and which is due to the relatively low frequency. At the frequency of 1 GHz,

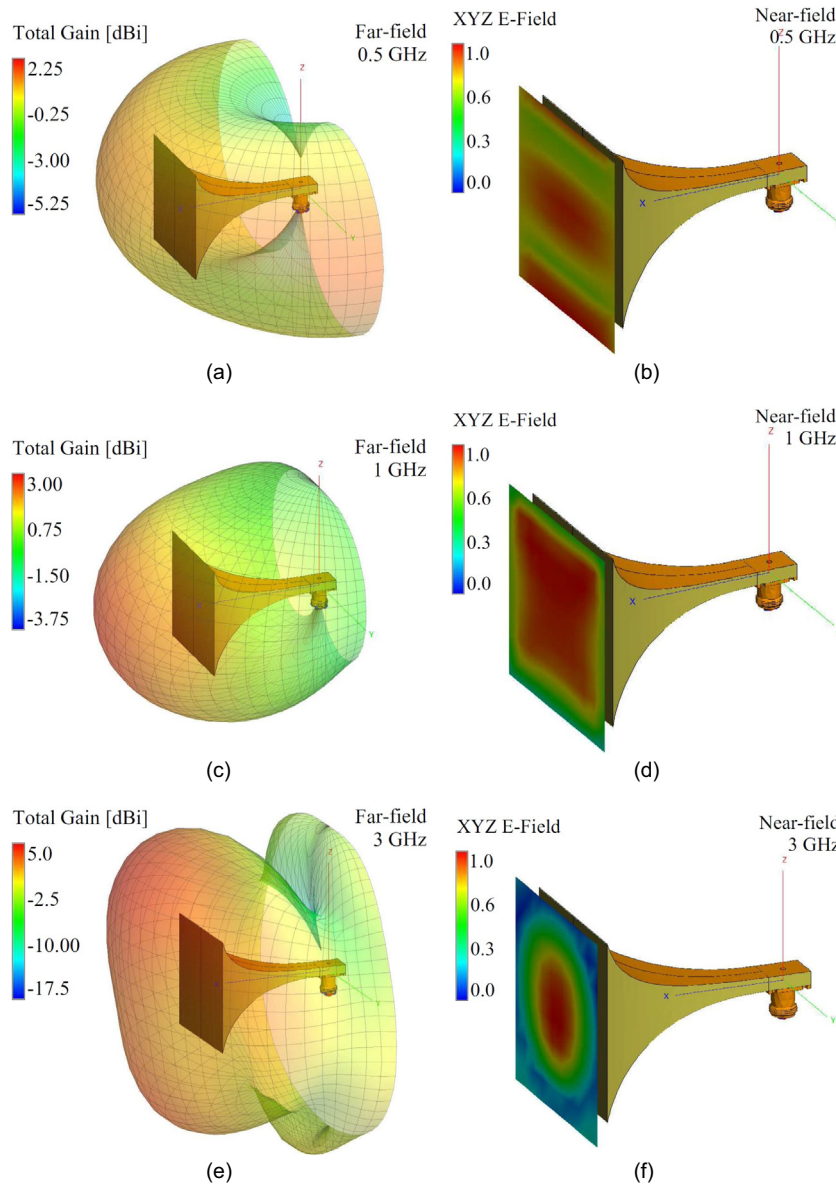


**Fig. 4.** Electromagnetic simulation using FEKO. Total gain in far-field [dBi] (on the left) and normalized electric field in E-plane (on the right) for the dielectric-coupled antenna for three different frequencies (0.5, 1 and 3 GHz).

both antennas appear more directive in their front parts and the maximum gain increases to 3.0 dBi. At the frequency of 3 GHz, we can already see side lobes at the antenna feeds. The air-coupled antenna is very directive for this frequency, the maximum gain reaches 10 dBi in the front part of the antenna. On the contrary, the directivity of the dielectric-coupled antenna is less significant with the maximum gain of 5 dBi which is on the upper front part on the antenna aperture (see Fig. 4e). The maximum values for the electric field in the E-plane are along the copper waveguides of the antennas for the air-coupled antenna for frequencies 0.5 and 1 GHz. For the same frequencies, the maximum electric field is distributed over a larger area in the central parts of the dielectric-coupled antenna. At 3 GHz, the maximum strength of the electric field is at the very mid part for both antennas. The return loss  $H_i$  of the antennas was simulated and compared with the measured values. It is displayed in Fig. 5 and explained in the following subsection.

### 2.3. Antenna calibrations

To see the real performances of the antennas, they were calibrated against a copper sheet using the antenna model of Lambot et al.

(2004); Lambot and André (2014). The antennas were fed by a vector network analyser (VNA, ZVB8, Rhode & Schwarz, Munich, Germany). A VNA is a technology allowing performing measurements in the frequency domain. It was connected to the antennas with a 50  $\Omega$  impedance coaxial cable. The VNA was calibrated using an Open-Short-Match reference calibration kit at the connection between the antenna and the coaxial cable. The operating frequency range was set to 0.5–3.5 GHz and the frequency step was fixed to 2 MHz. The antenna calibrations were performed by means of several measurements at different distances from a copper sheet (3×3 m) following the procedure described in Lambot et al. (Lambot et al., 2004; Lambot and André, 2014). The distance of the antennas from the copper sheet varied from 0 to 30 cm with 100 steps. Fig. 5 shows the measured frequency-dependent return loss  $H_i$  (red curve) and its phase, which is compared with the simulated values obtained by FEKO (blue curve).  $H_i$  corresponds to a free space measurement. Fundamentally, it represents the complex, frequency-dependent global reflection coefficient of the antenna for the fields incident from the antenna feed (see Lambot and André (2014) (Lambot and André, 2014)). Both antennas have the best performance in free-space when the magnitude of  $H_i$  is 0.5. The air-coupled antenna meets this

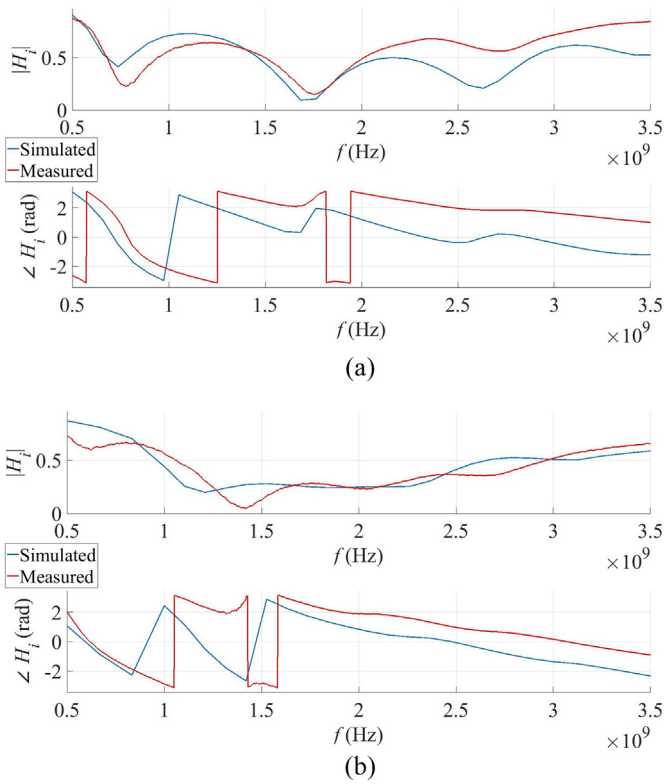


Fig. 5. Return loss transfer functions ( $H_i$ ) magnitude and phase for a) air-coupled antenna and b) dielectric-coupled antenna - simulated with FEKO (blue) and measured (red) in the frequency range 0.5–3.5 GHz. (For interpretation of the references to colour in this figure legend, the reader is referred to the web version of this article.)

requirement in free-space in the frequency range 1.5–2.5 GHz and the dielectric-coupled antenna meets this requirement in free-space in the frequency range 1.0–3.5 GHz. The performances of the dielectric-coupled antenna are expected to be better when coupled with a medium (especially a medium with  $\epsilon_r = 2.2$ ). Generally, both antennas have a significant performance in the whole frequency range. The measured and simulated values have similar trends, which indicates that the antennas assembly was successful.

2.4. Laboratory sandbox with a buried metallic bar

To further test the antennas, radar measurements were performed over a sandbox with a buried metallic bar. Both measurements were done directly after the antenna calibrations, so the same equipment and settings were used (VNA, ZVB8, Rhode & Schwarz, Munich, Germany). We performed the measurements at about 5 mm above the sand surface. The length of the profile was 2.0 m. The bar had a circular cross-section and its diameter was 4 cm. It was buried 10 cm under the sand surface. The configuration of the sandbox is displayed in Fig. 6. Both antennas served during the measurements as a transmitter and receiver (monostatic radar system).

Fig. 7 displays radar images obtained with both antennas. The time domain images were obtained from the frequency domain radar data using the inverse fast Fourier transform (IFFT). We can observe raw data (Fig. 7a and b) and two types of data processing. In the first case (Fig. 7c and d), the  $H_i$  subtraction was used, and in the second case (Fig. 7e and f), the average background subtraction (zero spatial frequency removal) was applied. For both processed images, an exponential gain function was used. In all cases (even for the raw data), we can observe the reflection hyperbola from the bar (position  $\approx 0.8$  m, time 2–2.5 ns) and the copper sheet reflection at the bottom of the radar image (at about 10 ns). These results demonstrate the functioning of both antennas for subsurface and material imaging. The reflection from the bar shows a

better contrast for the dielectric-filled antenna, thanks to the antenna-medium coupling. Yet, the sand being dry, i.e., with a relative permittivity of about 2.8, the results are also good for the air-filled antenna. In both cases, subtraction of the antenna free-space responses ( $H_i$ ) remove all inner antenna reflections that are independent of the target. Hence, the sand surface and deeper structures appear more clearly. The average subtraction removal also partly removed the sand surface reflection.

3. Lightweight radar system

In order to perform measurements during handheld applications quickly and easily, a lightweight radar system for an ergonomic manipulation was designed and assembled. It consists of a handheld VNA (Planar R54, Copper Mountain Technologies, Indianapolis, USA, <http://www.coppermountaintech.com/>). This device has relatively small dimensions ( $117 \times 39 \times 19$  mm) and with its weight of about 250 g it is relatively light. This VNA is capable of measuring through the 50  $\Omega$  1-port the reflection coefficient S11 from 85 MHz to 5.4 GHz. Its measurement speed is about 200  $\mu$ s per frequency. In order to perform measurements as precisely as possible, the VNA had to be calibrated using Open - Short - Match calibration standards. The VNA was controlled using an Intel Computer Stick with Windows 10 as operating system. To accomplish a remote control of this microcomputer and VNA, a custom program was written to be able to operate it with an external device (a remote computer, tablet or smartphone). We set up the radar remote controller using a Node.js web server application. The user interface consists of a web page (HTML and JavaScript) including displays and buttons. In particular, the buttons are used to communicate with the VNA through Python. The Intel Computer stick produces a Wi-Fi network to which any computer, smartphone or tablet can connect after writing a password. The internet browser of the smartphone is used to access the controlling webpage.

The positioning of the radar system consists of a webcam reading a rebar ruler which was developed for this application (see following subsection). The complete lightweight radar system with the barcode ruler is displayed in Fig. 8.

3.1. Barcode positioning system

In order to make the positioning system efficient, precise and easy to handle, we developed an automated reading algorithm to process a barcode ruler. The usage of the traditional positioning system (e.g., surveying wheel) was overcome for this kind of measurement because irregular shapes of surfaces do not often allow a good contact of the wheel with the surface and so, it cannot properly turn during the whole data acquisition. In those cases, remote positioning systems are more advantageous and in any case, lead to fewer interferences in the measurements. A 5 m long binary ruler with a resolution (step) of 5 mm was plotted with two boundary stripes (upper and lower) of the same width (see the black and the white stripes highlighted by black and red arrows in Fig. 9) for easier recognition of the barcode

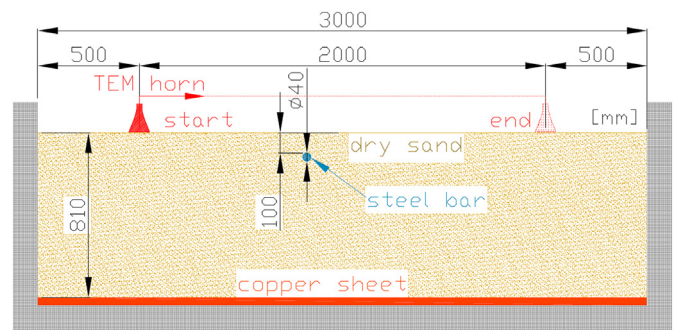
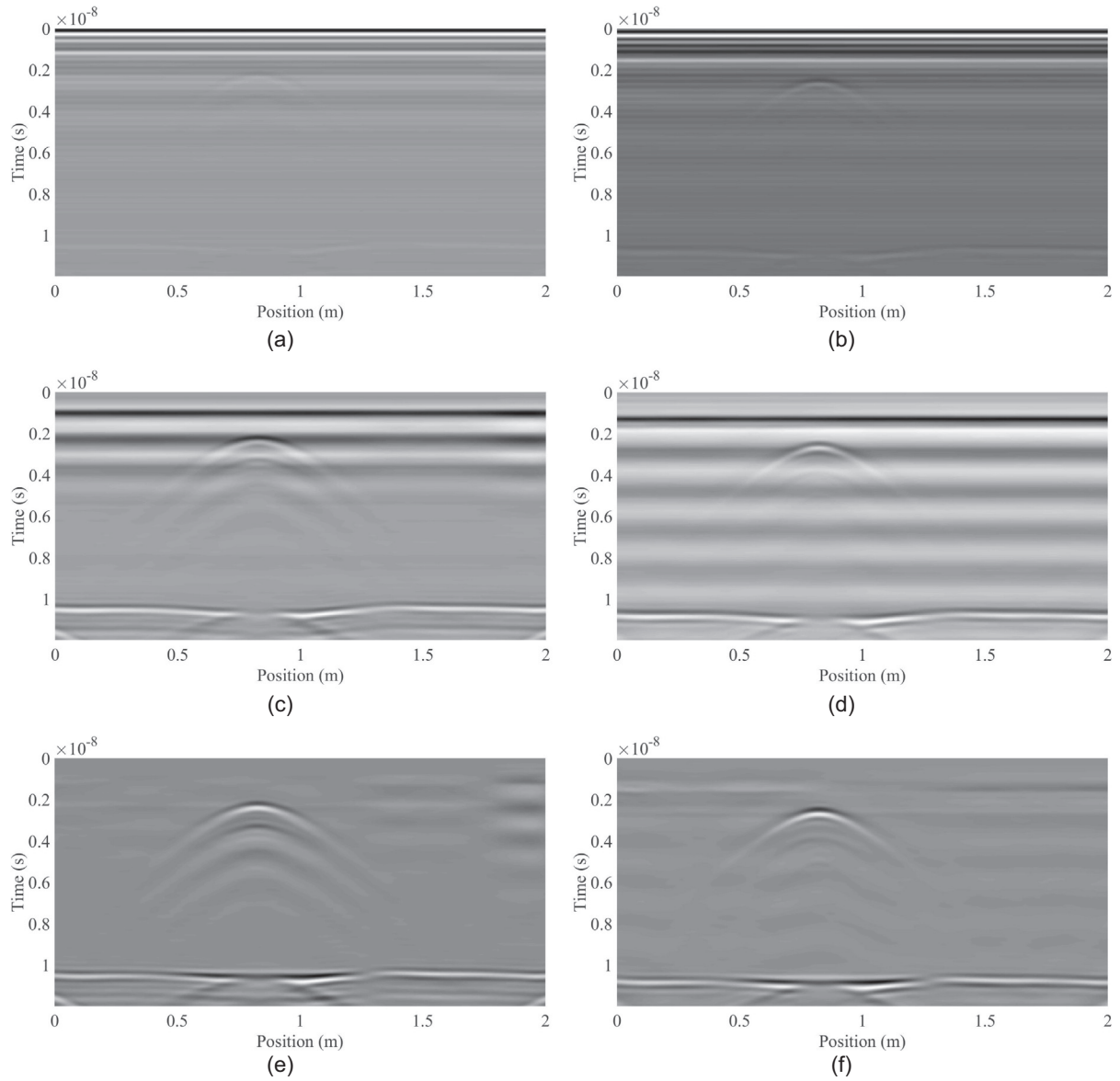


Fig. 6. Laboratory sandbox with a copper sheet on its bottom, filled with dry sand. A metal (steel) bar was buried approximately 10 cm under the sand surface. 2 m long radar measurements started and ended 50 cm from the box edges.



**Fig. 7.** Near-field measurement (5 mm) with the air-coupled (left) and dielectric-coupled (right) antennas over the sandbox with a buried metallic bar: a-b) Raw data, c-d) Hi subtraction, e-f) average background subtraction.

upper and lower borders. The resolution and the length of the ruler are, indeed, adaptable to a particular application. The binary ruler was developed for being fixed on the investigated medium (tree, column, wall) whilst a webcam (Logitech Webcam C170) installed on the antenna (15–20 cm away from the ruler) reads the ruler. The camera is controlled by a Python script executed on the Intel Computer in order to snap 2 frames per second which are subsequently saved on the SD memory card. In order to have high-quality pictures, it is essential to perform the movements with the radar system relatively slowly (to avoid recording blurred images).

The post-processing of the images was done in Matlab as well as the processing of the radar data. The raw images (see Fig. 10a as an example) are split into 3 colour channels (red, green, blue) to obtain the information richest green channel (see Fig. 10b) which contains twice as many pixels as the other channels and so, it contains less noise (Lakshmi et al., 2016; Kim, 2017). The matrix defining the selected green channel image is subsequently simplified to black and white colours (black = 0, white = 1), so the lighter parts of the image are represented by white and analogically, the darker parts of the image are represented by black. For better visibility in this paper (as the pages

are white), we used yellow instead of white and blue instead of black (see Fig. 10c). Then, the image is cleaned in order to get rid of some noise (see the differences between Fig. 10c and 10d). Because any picture is never perfectly straight, it is necessary to rotate it, so the stripes are horizontal (see Fig. 10e). Then, the lower and upper triangles originating from the rotation must be cut (see Fig. 10f). Due to the lowest degree of the image distortion in its centre, the middle part of the image/matrix was chosen for the final determination of the antenna position. The selected strip should not be too narrow (sensitivity to errors in single pixels) nor too wide (influence of the distortion of the edges), therefore the compromise was to select 10 columns on each side of the central pixel column (around 1% of the total number of columns), 21 in total (see Fig. 10g). At this stage, it is essential to determine the exact position of the barcode. The algorithm finds the bordering black stripes (see the red arrows in Fig. 10g), measures their width and determines the position of the following white stripes with the same dimension. Knowing the positions of the barcode edges, the matrix is cut, so only the part of the barcode remains in the image (see Fig. 10h). As the final decimal number of the ruler is a thirteen-digit binary number ( $5000_{\text{DEC}} = 1001110001000_{\text{BIN}}$  m), we split the final 21-column matrix

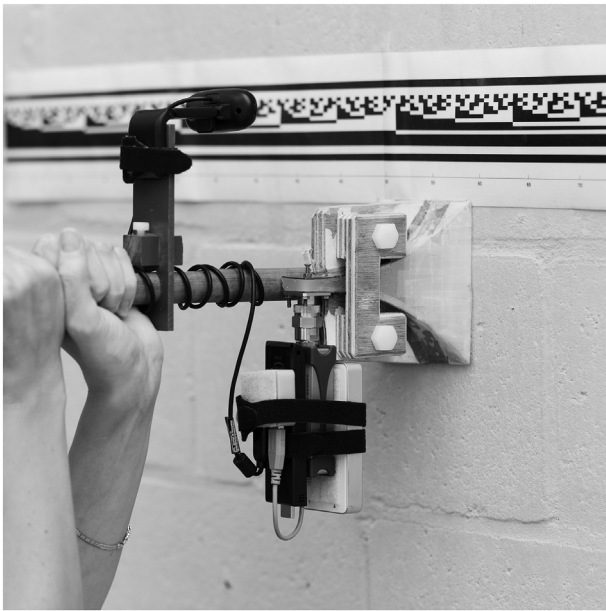


**Fig. 8.** The lightweight radar system including the dielectric coupled TEM horn antenna, handheld VNA, Intel computer, battery, positioning barcode and the webcam.

into 13 lines and to each row, we assign the most frequent pixel value (0 or 1). Hence, we obtain a matrix with 21 columns and 13 lines representing 21 binary numbers (see Fig. 10i). The same final matrix expressed with digits is shown in Fig. 10j. At this stage, the algorithm can read the 21 binary numbers from the bottom up.

Fig. 11 displays a bar chart with all 21 converted decimal numbers which were read from the final matrix in Fig. 10i. The positions marked by the red marks were indicated as an error which is usually caused by blurred transition between two positions on the barcode ruler (see detailed images of the barcode in Fig. 10g-i). Those positions were therefore automatically excluded from the position list and only the representative parts had to be selected for the position evaluation. The position list was processed in order to get a representing value by assessing the occurrence of the numbers and their medians.

The radar and positioning data were matched using the timestamps of the recorded files from the camera and the radar. Both acquisition systems (positioning and radar) were launched from the single computer (Intel Stick) which guaranteed the same time in both devices.

#### 4. Laboratory tests

##### 4.1. The lightweight radar waveforms

After the lightweight radar system assembly, two simple measurements were performed in order to analyse of the reflections at the

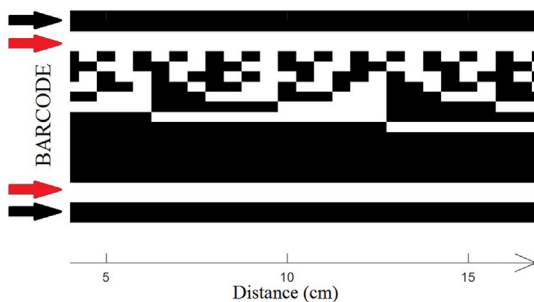


**Fig. 9.** A part of the generated barcode ruler with white (red arrows) and black (black arrows) stripes borders. In this example, the resolution of the barcode is 5 mm. (For interpretation of the references to colour in this figure legend, the reader is referred to the web version of this article.)

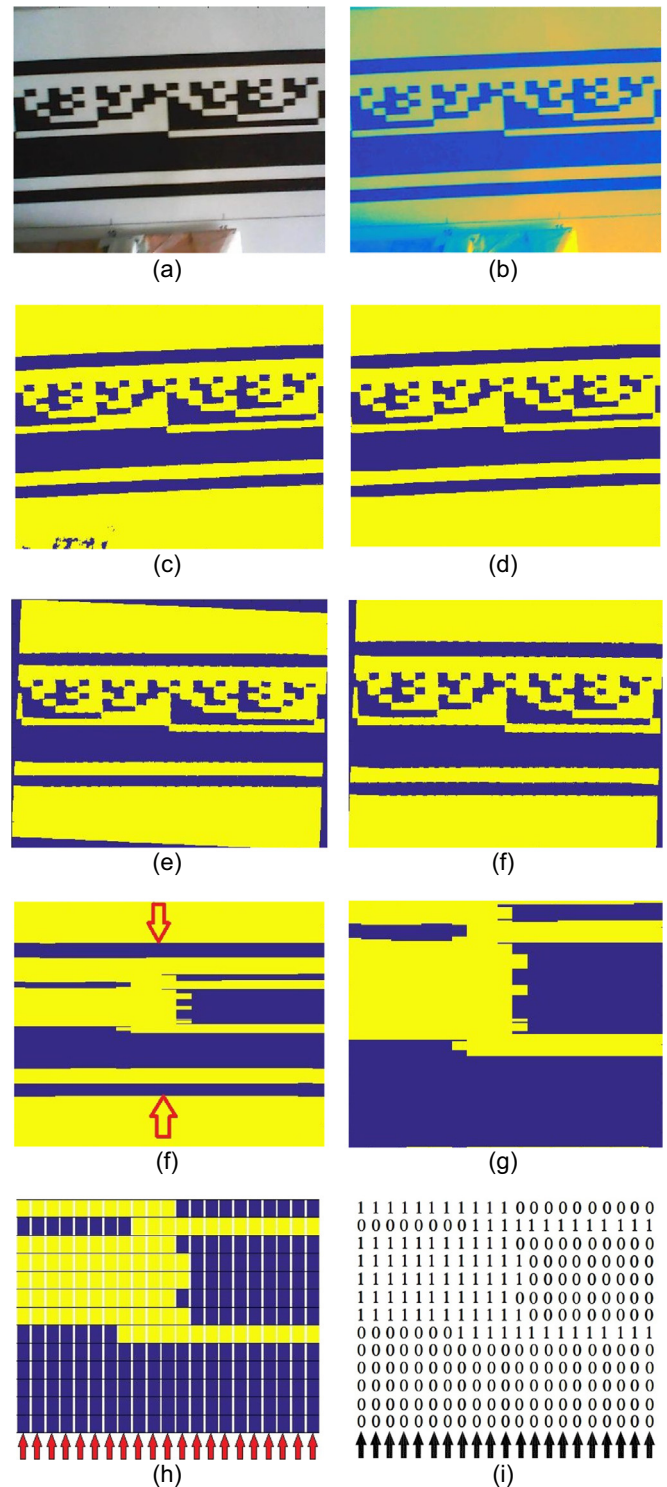


**Fig. 10.** (a): Raw image of the barcode ruler taken by the webcam, (b): Green channel of the image, (c): Simplified matrix of the green channel (0 = blue, 1 = yellow), (d): Cleared matrix (without noise), (e): Rotated image with horizontal stripes, (f): Rotated image without lower and upper triangles caused by the rotation, (g): Mid part of the matrix (21 columns), (h): Part of the matrix containing only the barcode, (i): 21-column matrix split into 13 lines representing 21 binary numbers, (j): Final matrix expressed in numbers. Each column represents a binary number (from bottom to top). (For interpretation of the references to colour in this figure legend, the reader is referred to the web version of this article.)

feed and at the antenna aperture. In particular, we compared: 1) free-space measurement, where the antenna was held several meters from metallic reflectors, 2) near-field measurement, where the antenna was

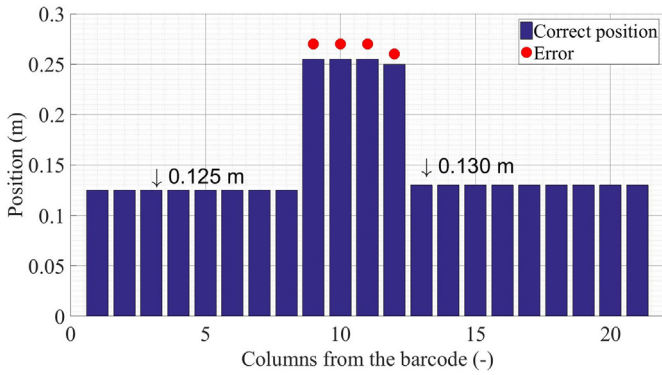


Fig. 11. Binary numbers converted into decimals. The transitions between two positions marked with red bullets were excluded from the position evaluation as they were indicated as an error. (For interpretation of the references to colour in this figure legend, the reader is referred to the web version of this article.)

laid down on a concrete floor. Both antennas (air-coupled and dielectric-coupled) were used in this experiment.

Fig. 12 shows the radar waveforms in the time domain of both air-coupled (blue) and dielectric coupled (red) antennas for: a) free-space, b) in the near-field over a concrete floor. At the beginning (less than 0.5 ns), we can see negative peaks for both measurements. These reflections correspond to the transition from the antenna connector to the feed and they are comparable for both antennas for both measurements (of course, in the dielectric the signal propagates slower than in

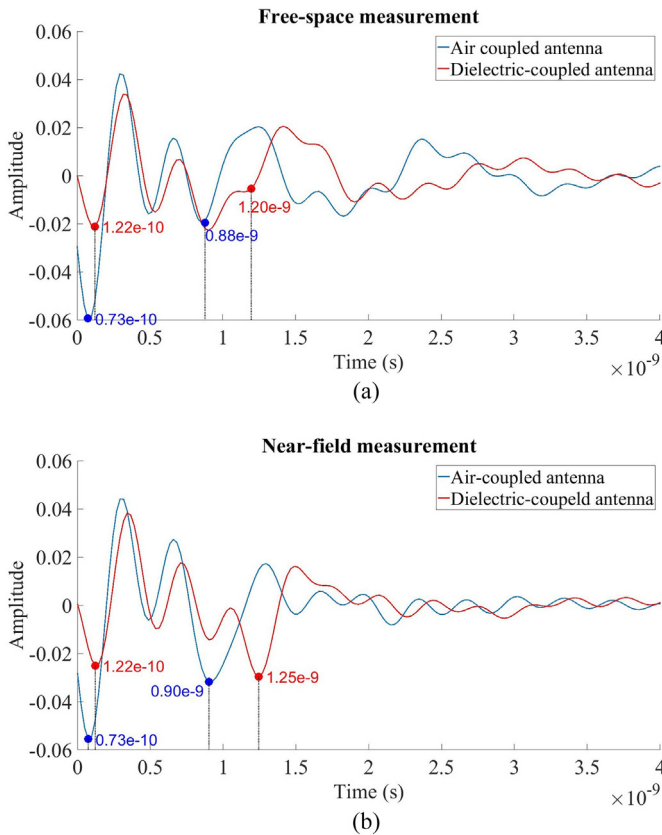


Fig. 12. Waveform comparisons of the air-coupled (blue) and the dielectric-coupled (red) antennas: a) free-space measurement, b) near-field measurement (0 nm from the surface) on a concrete floor. In both figures, the first marked peaks (below 0.5 ns) point approximately at the reflections at the antenna feed, the second marked peaks ( $1 \text{ ns} \pm 0.25 \text{ ns}$ ) point approximately at the antenna aperture. (For interpretation of the references to colour in this figure legend, the reader is referred to the web version of this article.)

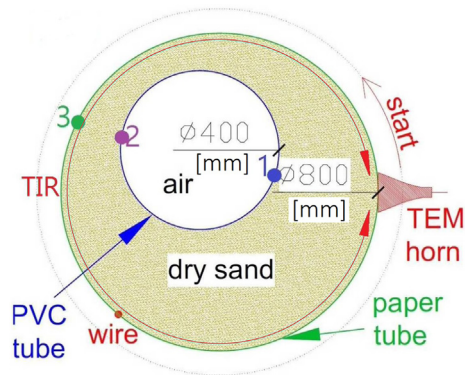


Fig. 13. Configuration of the laboratory cylindrical model. A plastic cylinder ( $D = 0.4 \text{ m}$ ) was placed off-centre in a paper cylinder ( $D = 0.8 \text{ m}$ ), the space between them was filled with dry sand. Points 1, 2, 3 and the path of the TIR (total internal reflection) correspond to the reflection curves in Fig. 17.

air and so, the reflection is slightly postponed from 0.073 to 0.122 ns). The second remarkable reflection occurs at the antenna aperture. The peaks of the air-coupled antenna (blue curve) have negative values in both measurements and it occurs at  $\approx 0.9 \text{ ns}$ . The antenna aperture reflection of the dielectric-coupled antenna (red curve) has a shape which is different for both free-space and near-field measurements. We can observe a very similar trend for both measurements until  $\approx 0.9 \text{ ns}$ , then the signal hits two different media: a) air with the  $\epsilon_r \approx 1$  which is smaller than the dielectric (wax) with  $\epsilon_r \approx 2.2$ , b) concrete with  $\epsilon_r \approx 4.5$  which is larger than the dielectric (wax)  $\epsilon_r \approx 2.2$ . The different electromagnetic properties of the media cause inversion of the signal peak, as described by Rial et al. (2009). Nevertheless, the waveform in the near-field with numerous reflections is very complex. These observation times are therefore very approximate. For this paper, the position of the antenna aperture reflections in the radar images was necessary to correctly determine undersurface structures of observed objects (air-coupled 0.9 ns, dielectric-coupled 1.25 ns).

4.2. Laboratory tree trunk model

The next step after the simulations and calibrations was testing the radar system in more realistic conditions. We tested the radar system



Fig. 14. Laboratory column consisting of an outer paper tube, inner plastic tube and dry sand between both tubes (see Fig. 13).

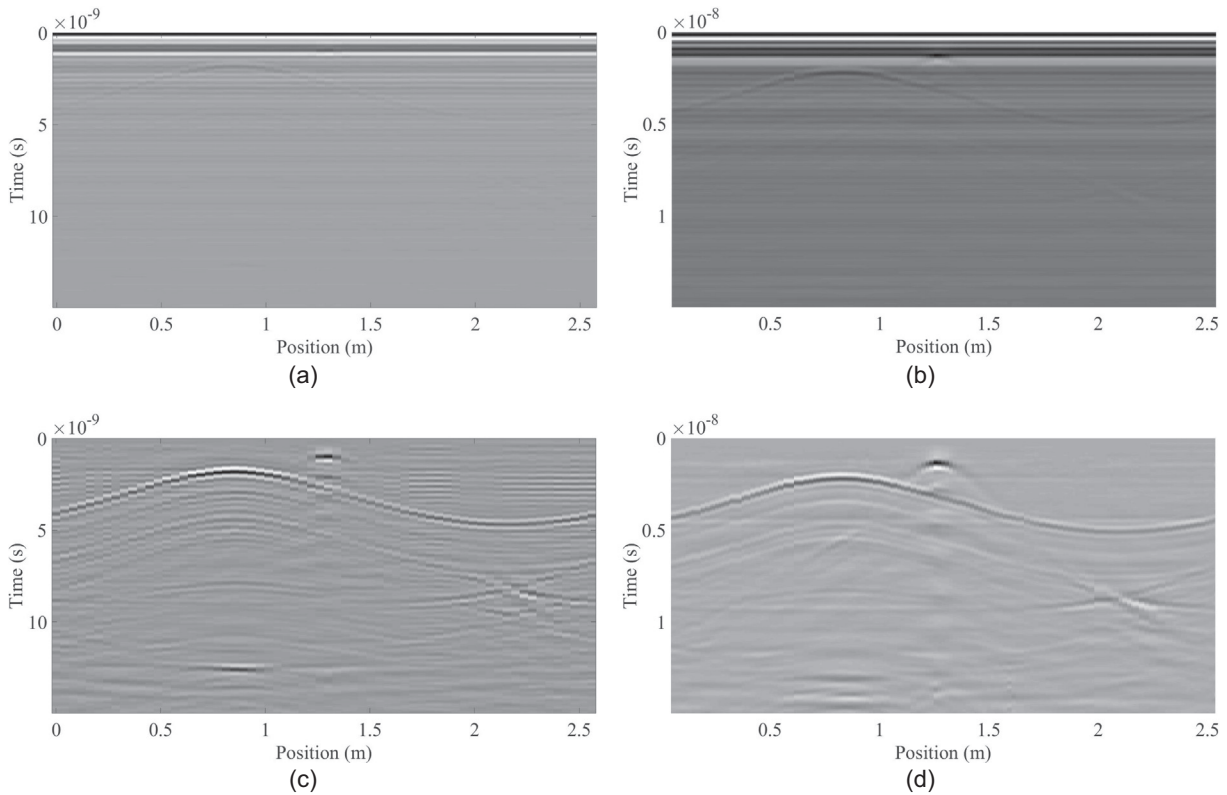


**Fig. 15.** Radar images of the near-field measurements (0 mm) with the air-coupled (left) and dielectric-coupled (right) antennas around the laboratory cylindrical model: a-b) Raw data, c-d) average background subtraction with an exponential gain function.

and antennas on a laboratory cylindrical model composed of two plastic and paper tubes filled with dry sand (see its configuration in Fig. 13) to inspect the visibility of the internal void (the empty tube) as in our previous experiments (Ježová et al., 2018). The laboratory model was 1.8 m high and it is shown in Fig. 14. Before the measurement, the barcode ruler was fixed on the model to provide the positioning information. The frequency range for this experiment was 0.5–3.5 GHz as well.

In Fig. 15, two near-field measurements (0 mm from the surface) are shown. The first one was done with the air-coupled antenna (on the left) and the second one was done with the dielectric-coupled antenna (on the right). The first pair of images (Fig. 15a and b) show the raw

radar images without any signal processing. Both radar images are dominated by the antenna internal reflections. Nevertheless, in both of them, we can observe a very slight sinusoidal curve corresponding to the internal void. The lower two images (Fig. 15c and d) show the radar data processed with average background subtraction and with an exponential gain function. In those two images, we can clearly see the reflection curve corresponding to the beginning of the inner tube (see points 1 and 2 in Fig. 13), the opposite side of the outer tube (see point 3 in Fig. 13) and the total internal reflection (signal reflection along the inner edge of the outer tube, see Ježová et al. (Ježová et al., 2016)). These reflection curves are simplified in Fig. 17. Furthermore, in both processed images, we can observe a hyperbolic reflection at position 1.3–1.4 m and time 1 ns. It is a reflection originating from a metallic wire which was a part of the paper tube (see its position in Fig. 13) and was discovered after the model assembling. Both antennas

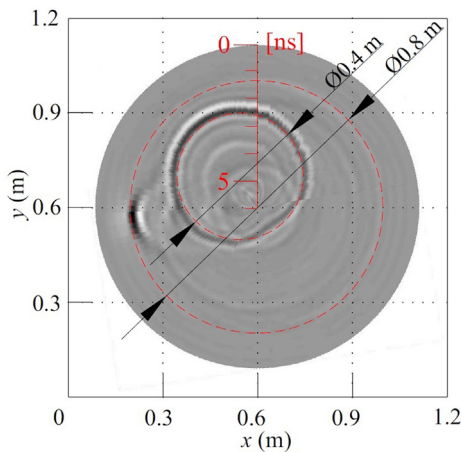


**Fig. 16.** A polar representation of the near-field radar image obtained with the dielectric coupled antenna around the laboratory cylindrical model (Ježová and Lambot, 2019). Average background subtraction and an exponential gain function were used to process the image. This polar representation corresponds to the radar image displayed in Fig. 15d.

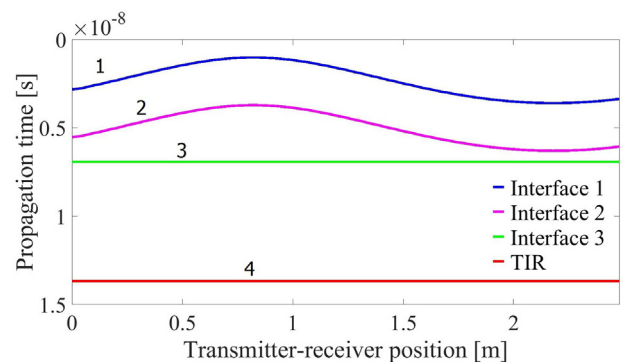


**Fig. 17.** Simulated reflection curves for the configuration shown in Fig. 13. In this image, the surface reflection was neglected.

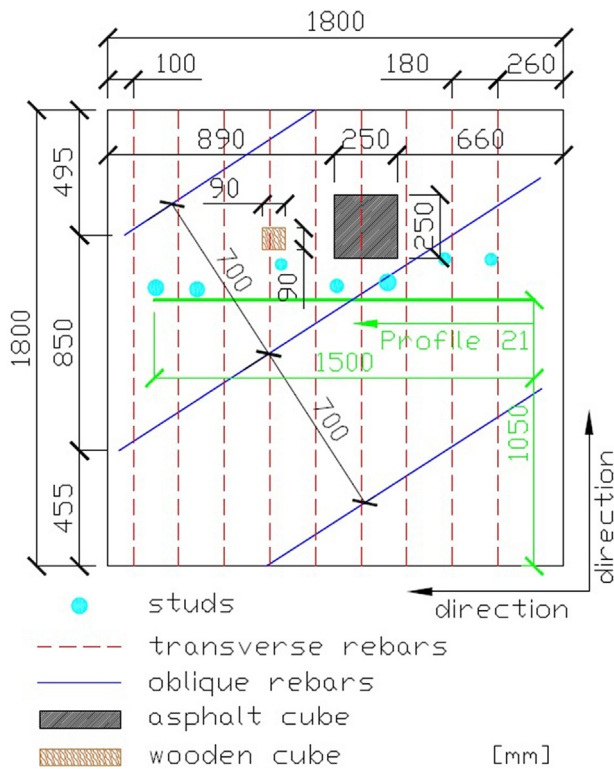


**Fig. 18.** The concrete structure plan with transverse and oblique metal rebars, asphalt and wooden cube and several studs.

provided very satisfactory radar images and the lightweight radar system proved its ease of use.

To better understand the GPR images, a polar representation of Fig. 15d obtained with the dielectric coupled antenna around the laboratory cylindrical model presented in our previous research (Ježová and Lambot, 2019) is displayed in Fig. 16.

## 5. Concrete rebars detection

We tested the radar system on a known concrete block at the Belgian Road Research Center (Brussels, Belgium). The concrete block was 1.8 m wide and 1.8 m long (see its configuration in Fig. 18), nevertheless, only approximately  $1.5 \times 1.5$  m of the area was investigated in order to avoid edge effects. The measurements were performed with the antenna in contact with the medium.

Fig. 19 shows an example of a radar profile (corresponding to profile 21 in Fig. 18) acquired over the concrete block with both the air-coupled and dielectric coupled antennas operating in the range 0.5–3.5 GHz. The raw data are displayed in Fig. 19a and b and, as well as during the laboratory tests, we can slightly see the buried structures, especially with the dielectric antenna. For both sets of data, average background subtraction and an exponential gain function were also applied (Fig. 19c and d). The surface reflection is present at about 1.0 ns for the air-coupled antenna and at about 1.3 ns for the dielectric antenna. From 2.5 to 2.8 ns, we can see 8 hyperbolas corresponding to the metallic bars - transverse reinforcement. Both surface and reinforcement reflections are highlighted by a red line and red rings, respectively. The data obtained by the dielectric-coupled antenna were of better quality, as they were less noisy. It is partly to be attributed to the better matching of the dielectric-coupled antenna with the concrete surface (this fact was less significant for the dry sand cases presented above).

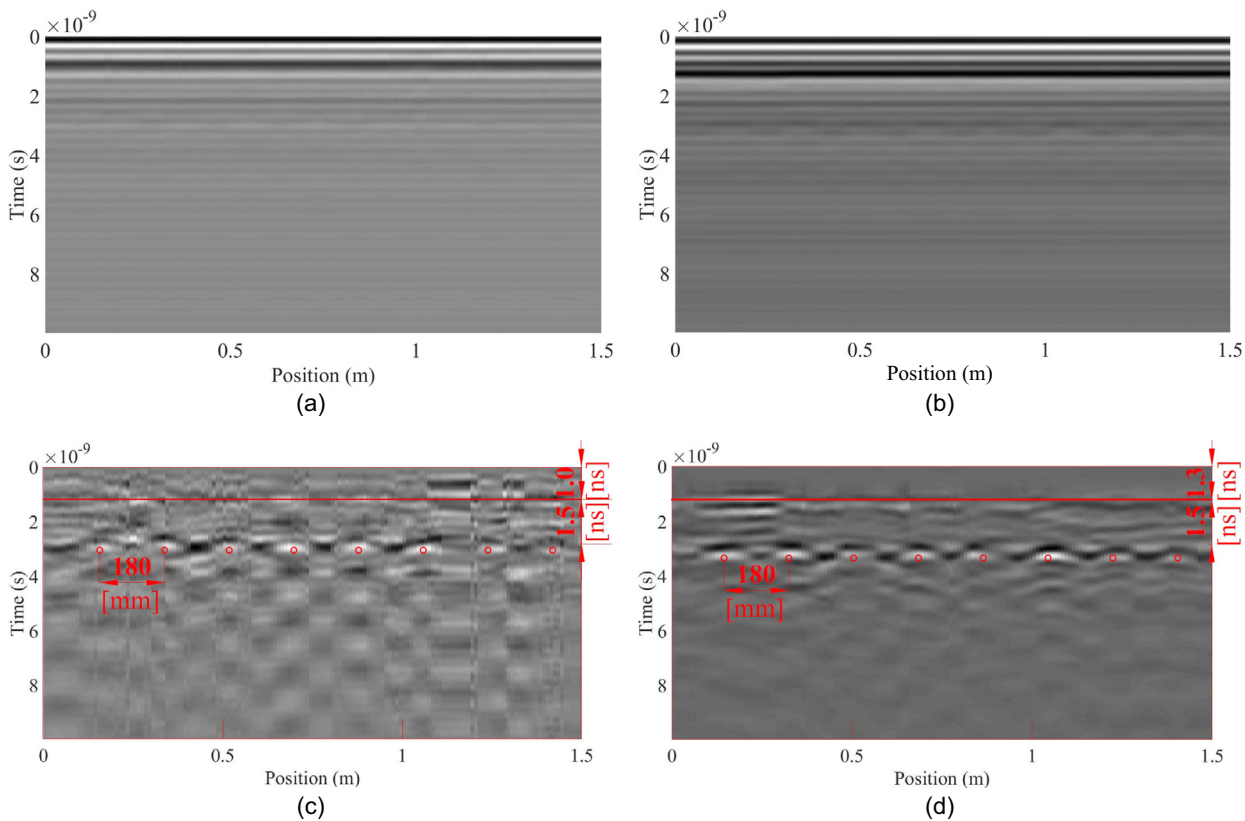


**Fig. 19.** Radar images of the near-field measurements (0 mm) with the air-coupled (left) and dielectric-coupled (right) antennas over the concrete block with buried transverse reinforcement corresponding to profile 21 in Fig. 18: a-b) Raw data, c-d) background subtraction with an exponential gain function. 1.0/1.3 ns - surface reflection/antenna aperture reflection, 2.5/2.8 ns - 8 hyperbolas corresponding to the concrete reinforcement.

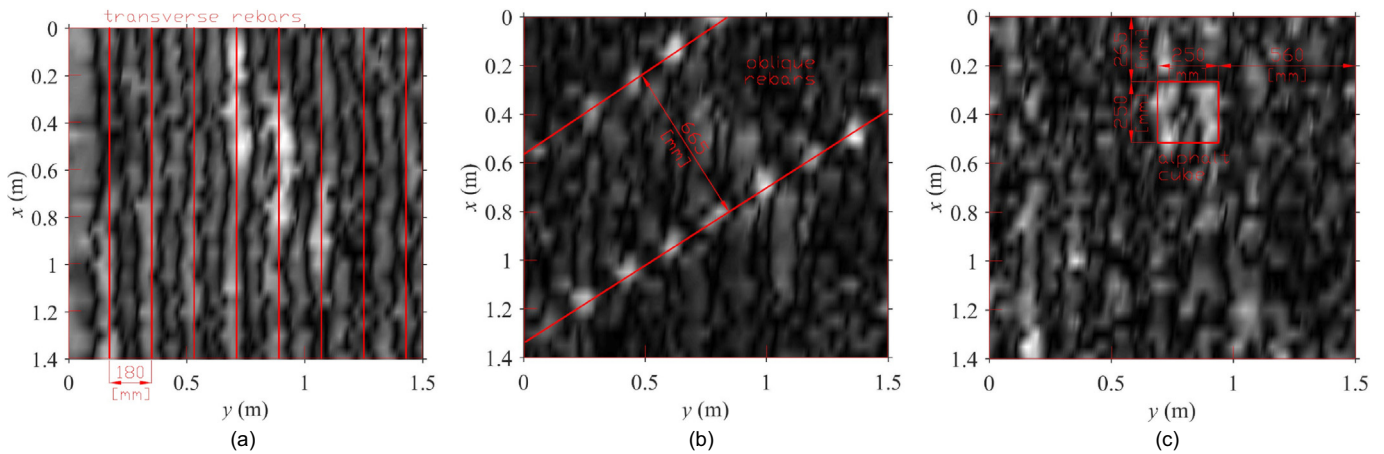


**Fig. 20.** The radar horizontal slices of the concrete block. a) 2.8 ns (10 cm under the surface) transverse rebars, b) 3.5 ns (15 cm under the surface) - oblique rebars, c) 4.1 ns (20 cm under the surface) - asphalt cube.

The 3D scan of the whole concrete block was done with the dielectric-coupled antenna providing better results. We performed 30 parallel profiles separated by 5 cm (see the directions in Fig. 18) with the velocity of the data acquisition of 4–5 measurements per second. This rate is determined by the microcomputer-VNA limitation. During evaluation of the radar profile 21 (in Fig. 19d), only the transverse reinforcement is visible. Nevertheless, during depth slicing of the 3D data set, several subsequent structures appeared. Fig. 20 shows three radar horizontal slices of the concrete block at: a) 2.8 ns, b) 3.5 ns, c) 4.1 ns. The first image displays the radar image slice at 2.8 ns (which corresponds to  $\approx 11$  cm under the concrete surface) and shows 8 transverse rebars with the positions corresponding to those in the plan of the block. Then, in the second image, which shows the radar image slice at 3.5 ns (corresponding to  $\approx 15$  cm under the surface), we can see oblique rebars which were not visible in the 2D radar profile. Finally, the third image shows the slice at 4.1 ns (corresponding to  $\approx 20$  cm under the surface) where we can see very well square reflections corresponding to the place where an asphalt cube is placed. The reflections were highlighted by the red lines in the radar slices. The transverse rebar reflections correspond very well to the reality (see Fig. 18) with their span (180 cm) and also their depth (11 cm). We detected only two oblique rebars (out of three) and their span seems to be smaller in the radar data compared to the reality (66.5 cm compared to 70 cm). They should be present at the depth of 12 cm, nevertheless, in our data, they appear at about 15 cm. Finally, the presence of the asphalt cube was determined very precisely in terms of its size (25  $\times$  25 cm) and its depth (about 20 cm). In the radar data, the wooden cube and spuds were not detected. As the depth of the concrete rebars was slightly changing and given the chosen horizontal depth slice, the additional stripes observed partly correspond to the reflection hyperbola branches. That is why some rebar reflections may appear duplicated.

## 6. Summary and Conclusions

We designed a radar system with a lightweight vector network analyser and two horn antennas, namely, an air-coupled and a dielectric-coupled horn. Both antennas were designed following the antennas of Mallahzadeh and Karshenas (2009). The dielectric-coupled TEM horn was designed in order to obtain better coupling between an investigated medium surface and the antenna. In order to do so, paraffin wax was chosen as dielectric because of its electromagnetic and mechanical properties. In order to perform measurements as easily as possible, the lightweight radar system including the antenna, the handheld VNA, the controlling device - Intel Stick computer, the external battery and the positioning camera was designed and assembled. The whole

radar system was controlled by a special mobile application developed by the authors. The size of the VNA is 117  $\times$  39  $\times$  19 mm and its weight is about 250 g, its measurement speed is about 200  $\mu$ s per frequency.

The antennas were simulated using FEKO software. The isotropic gain of the antennas was simulated. Both antennas showed good directivity in the front part, especially above 1 GHz. Before the antennas were used with the lightweight radar system, they were calibrated against a copper sheet. Their return loss  $H_r$  was evaluated and compared with simulated data. The air-coupled antenna had  $H_r < 0.5$  in the frequency range 1.5–2.5 GHz and the dielectric-coupled antenna met this requirement in the frequency range of 1.0–3.5 GHz. Then, some laboratory testing measurements were performed. We inspected a laboratory sandbox with a buried metal bar. Subsequently, we did a laboratory measurement around a cylindrical column model filled with sand. Both antennas demonstrated good performances with better results achieved with the dielectric horn.

Then, a field measurement of a concrete block with a known structure was done from above. The radar profiles of both antennas showed the undersurface reinforcement, nevertheless, the dielectric-coupled antenna showed slightly better performance. Hence, it was selected for the 3D scan of the concrete block. In particular, 30 profiles separated by 5 cm were scanned in order to get a 3D view of the concrete block.

The dielectric antenna proved better performance during all experiments accomplished in this paper. It is caused by the better coupling of the antenna with the surface of the investigated objects. The lightweight radar system with a dielectric-coupled TEM horn antenna and with a remote positioning system with a webcam proved good functionality as it was very easy to handle and as it provided satisfactory results.

In future, the lightweight radar system will be used to walls, columns and especially tree trunk inspection where the coupling of the antenna with the surface is fundamental.

## Acknowledgment

The authors would like to acknowledge the support of the Fonds de la Recherche Scientifique (FNRS), Belgium, through the SENSWOOD project (Convention no 19526260). This research was also carried out within the framework of EU funded COST Action TU 1208 “Civil Engineering Applications of Ground Penetrating Radar”. The authors would also like to thank the Belgian Road Research Center (BRRC) for providing the concrete structure with known interior.

## References

- Al Hagrey, S.A., 2007. Geophysical imaging of root-zone, trunk, and moisture heterogeneity. *J. Exp. Bot.* 58 (4), 839–854.

- Alani, A.M., Tosti, F., 2018. GPR applications in structural detailing of a major tunnel using different frequency antenna systems. *Constr. Build. Mater.* 158, 1111–1122. <https://doi.org/10.1016/j.conbuildmat.2017.09.100>.
- André, F., van Leeuwen, C., Saussez, S., Durmen, R.V., Bogaert, P., Moghadas, D., de Ressaiguier, L., Delvaux, B., Vereecken, H., Lambot, S., 2012. High-resolution imaging of a vineyard in south of France using ground-penetrating radar, electromagnetic induction and electrical resistivity tomography. *J. Appl. Geophys.* 78 (Supplement C), 113–122.
- Angelis, D., Tsourlos, P., Tsokas, G., Vargemezis, G., Zacharopoulou, G., Power, C., 2018. Combined application of GPR and ERT for the assessment of a wall structure at the Heptapyrgion fortress (Thessaloniki, Greece). *J. Appl. Geophys.* 152, 208–220. <https://doi.org/10.1016/j.jappgeo.2018.04.003>.
- Annan, A.P., 2002. GPR - history, trends, and future. *Subsurf. Sens. Technol. Appl.* 3 (4), 253–270.
- Ardekani, M.R.M., Jacques, D.C., Lambot, S., 2016. A layered vegetation model for GPR full-wave inversion. *IEEE J. Sel. Topics Appl. Earth Observ. Remote Sens.* 9 (1), 18–28.
- Ascama, H.D.O., Hiramatsu, R.K., De Oliveira, A.M., Dionisio, C.R.P., Kofuji, S.T., 2013. Simulation and manufacturing of a miniaturized Exponential UWB TEM horn antenna for UWB Radar applications. *J. Microw. Optoelectron. Electromagn. Appl.* 12 (2), 655–665.
- Bassam, S., Rashed-Mohassel, J., 2006. A Chebyshev tapered TEM horn antenna. *PIERS Online* 2 (January 2006), 706–709.
- Benedetto, A., Tosti, F., Ciampoli, L.B., D'Amico, F., 2017. An Overview of Ground-Penetrating Radar Signal Processing Techniques for Road Inspections, *Signal Processing* 132 (Supplement C), pp. 201–209.
- Bird, T.S., Antengenuity, P., Fellow, C., Granet, C., 2013. *Profiled Horns and Feeds, Handbook of Reflector Antennas and Feed Systems Volume II: Feed Systems*, pp. 123–156.
- Casas, A., Pinto, V., Rivero, L., 2000. Fundamental of ground penetrating radar in environmental and engineering applications. *Ann. Geophys.* 43 (6). <https://doi.org/10.4401/ag-3689>.
- Congedo, F., Monti, G., Tarricone, L., 2010. Modified bowtie antenna for GPR applications. *Proceedings of the XIII International Conference on Ground Penetrating Radar*, pp. 1–5 <https://doi.org/10.1109/ICGPR.2010.5550127>.
- Daniels, J.J., 2000. *Ground Penetrating Radar Fundamentals*, USEPA Publication (Appendix), pp. 1–21.
- Foster, P., Tun, S., 1995. A Wideband Balun from Coaxial Line to TEM Line, *Antennas and Propagation* (Figure 3), pp. 4–7.
- Grosvenor, C.A., Johnk, R.T., Novotny, D.R., Canales, S., Davis, B., Veneman, J., 2007. *TEM Horn Antenna Design Principles*. National Institute of Standards and Technology.
- Hong, W.T., Kang, S., Lee, S.J., Lee, J.S., 2018. Analyses of GPR signals for characterization of ground conditions in urban areas. *J. Appl. Geophys.* 152, 65–76. <https://doi.org/10.1016/j.jappgeo.2018.03.005>.
- Ježová, J., Lambot, S., 2019. Influence of bark surface roughness on tree trunk radar inspection. *Ground Penet. Radar* 2 (1), 1–25. <https://doi.org/10.26376/GPR2019001>.
- Ježová, J., Mertens, L., Lambot, S., 2016. Ground-penetrating radar for observing tree trunks and other cylindrical objects. *Constr. Build. Mater.* 123, 214–225.
- Ježová, J., Lambot, S., Fedeli, A., Randazzo, A., 2017. Ground-penetrating radar for tree trunk investigation. *2017 9th International Workshop on Advanced Ground Penetrating Radar (IWAGPR)*, pp. 1–6 <https://doi.org/10.1109/IWAGPR.2017.7996079>.
- Ježová, J., Harou, J., Lambot, S., 2018. Reflection waveforms occurring in bistatic radar testing of columns and tree trunks. *Constr. Build. Mater.* 174, 388–400. <https://doi.org/10.1016/j.conbuildmat.2018.04.128>.
- Jonard, F., Weihermá, L., 2012. Müller, H. Vereecken, S. Lambot, Accounting for soil surface roughness in the inversion of ultrawideband off-ground GPR signal for soil moisture retrieval. *Geophysics* 77 (1), H1–H7.
- Kao, C., Li, J., Liu, R., Cai, Y., 2008. Design and analysis of UWB TEM horn antenna for ground penetrating radar applications. *IGARSS 2008–2008 IEEE International Geoscience and Remote Sensing Symposium*. 4, pp. IV - 569–IV - 572. <https://doi.org/10.1109/IGARSS.2008.4779785>.
- Karshenas, F., Mallahzadeh, A.R., Imani, A., 2009. Modified TEM horn antenna for wide-band applications. *Proceedings - 2009 13th International Symposium on Antenna Technology and Applied Electromagnetics and the Canadian Radio Sciences Meeting, ANTEM/URSI*. 2009, pp. 6–10.
- Khalaj Amineh, R., Trehan, A., Nikolova, N.K., 2009. TEM Horn Antenna for Ultra-Wide Band Microwave Breast Imaging. *Prog. Electromagn. Res. B* 13, 59–74.
- Kilic, G., Eren, L., 2018. Neural network based inspection of voids and karst conduits in hydro-electric power station tunnels using GPR. *J. Appl. Geophys.* 151, 194–204. <https://doi.org/10.1016/j.jappgeo.2018.02.026>.
- Kim, S., 2017. Color image enhancement using subsampled channel difference. *Int. J. Sig. Proc. Image Proc. Patt. Recogn.* 10, 141–156. <https://doi.org/10.14257/ijsp.2017.10.7.13>.
- Lakshmi, M., Senthilkumar, J., Suresh, Y., 2016. Visually lossless compression for bayer color filter array using optimized vector quantization. *Appl. Soft Comput.* 46, 1030–1042. <https://doi.org/10.1016/j.asoc.2015.12.025>.
- Lambot, S., André, F., 2014. Full-wave modeling of near-field radar data for planar layered media reconstruction. *IEEE Trans. Geosci. Remote Sens.* 52 (5), 2295–2303. <https://doi.org/10.1109/TGRS.2013.2259243>.
- Lambot, S., Slob, E.C., Van Bosch, I.D., Stockbroeckx, B., Vanclooster, M., 2004. Modeling of ground-penetrating radar for accurate characterization of subsurface electric properties. *IEEE Trans. Geosci. Remote Sens.* 42 (11), 2555–2568.
- Lestari, A.A., Yarovoy, A.G., Ligthart, L.P., 2000. Adaptive antenna for ground penetrating radar. *Proc. SPIE 4084, Eighth International Conference on Ground Penetrating Radar*.
- Liu, Y., Shi, Z., Wang, B., Yu, T., 2018. GPR impedance inversion for imaging and characterization of buried archaeological remains: a case study at Mudu city site in Suzhou, China. *J. Appl. Geophys.* 148, 226–233. <https://doi.org/10.1016/j.jappgeo.2017.12.002>.
- Malherbe, J.A.G., Barnes, N., 2007. TEM horn antenna with an elliptic profile. *Microw. Opt. Technol. Lett.* 49 (12), 1548–1551 (arXiv:0604155).
- Malherbe, J.A.G., Barnes, N., 2007. TEM horn antenna with an elliptic profile. *Microw. Opt. Technol. Lett.* 49 (7), 1548–1551. <https://doi.org/10.1002/mop.22488>.
- Mallahzadeh, A.R., Karshenas, F., 2009. Modified TEM Horn Antenna for Broadband applications. *Prog. Electromagn. Res.* 90, 105–119.
- Mallahzadeh, A.R., Dastranj, A.A., Hassani, H.R., 2008. A novel dual-polarized double-ridged horn antenna for wideband applications. *Prog. Electromagn. Res. B* 1, 67–80.
- Manteghi, M., Rahmat-Samli, Y., 2004. A novel UWB feeding mechanism for the TEM horn antenna, reflector IRA, and the Vivaldi antenna. *IEEE Antennas Propag. Mag.* 46 (5), 81–87.
- Nichols, P., McCallum, A., Lucke, T., 2017. Using ground penetrating radar to locate and categorise tree roots under urban pavements. *Urban For. Urban Green.* 27, 9–14. <https://doi.org/10.1016/j.ufug.2017.06.019>.
- Persico, R., Gennarelli, G., Soldovieri, F., 2014. GPR prospecting on circular surfaces: Preliminary results. *Proceedings of the 15th International Conference on Ground Penetrating Radar*, pp. 79–82.
- Qi, M.Q., Tang, W.X., Ma, H.F., Pan, B.C., Tao, Z., Sun, Y.Z., Cui, T.J., 2015. Suppressing Side-Lobe Radiations of Horn Antenna by Loading Metamaterial Lens. *Sci. Rep.* 5, 9113–9118.
- Qin, H., Xie, X., 2016. Design and test of an improved dipole antenna for detecting enclosure structure defects by cross-hole GPR. *IEEE J. Select. Topics Appl. Earth Observ. Remote Sens.* 9 (1), 108–114. <https://doi.org/10.1109/JSTARS.2015.2466450>.
- Reci, H., Ma, T.C., Sbarta, Z.M., Pajewski, L., Kiri, E., 2016. Non-destructive evaluation of moisture content in wood using ground-penetrating radar. *Geosci. Instrum. Methods Data Syst.* 5 (2), 575–581. <https://doi.org/10.5194/gi-5-575-2016>.
- Rial, F.I., Lorenzo, H., Pereira, M., Armesto, J., 2009. Waveform analysis of UWB GPR antennas. *Sensors*, 1454–1470 <https://doi.org/10.3390/s90301454>.
- Rodríguez-Abad, I., Martínez-Sala, R., García-García, F., Capuz-Lladro, R., 2010. Non-destructive methodologies for the evaluation of moisture content in sawn timber structures: ground-penetrating radar and ultrasound techniques. *Near Surf. Geophys.* 8, 475–482.
- Sarkis, R., Craeye, C., 2010. Circular array of wideband 3d vivaldi antennas. *2010 URSI International Symposium on Electromagnetic Theory*, pp. 792–794.
- Sato, M., Fujiwara, J., Feng, X., Zhou, Z.-S., Kobayashi, T., 2005. Evaluation of a hand-held GPR md sensor system (alis). *IARP International Workshop on Robotics and Mechanical Assistance in Humanitarian Demining (HUDEM2005)*.
- Sato, M., Yokota, Y., Takahashi, K., Grasmueck, M., 2012. Landmine detection by 3D GPR system. *Proceedings of SPIE - the International Society for Optical Engineering*. vol. 8357, 835710. <https://doi.org/10.1117/12.918517>.
- Savelyev, T.G., van Kempen, L., Sahli, H., Sachs, J., Sato, M., 2007. Investigation of time-frequency features for GPR landmine discrimination. *IEEE Trans. Geosci. Remote Sens.* 45 (1), 118–129. <https://doi.org/10.1109/TGRS.2006.885077>.
- Weilin Li, Z.X., Jian Wen, S. Xu, 2018. Application of ground-penetrating radar for detecting internal anomalies in tree trunks with irregular contours. *Sensors* 18 (649).
- Wiesbeck, W., Adamiuk, G., Sturm, C., 2009. Basic properties and design principles of UWB antennas. *Proc. IEEE* 97 (2), 372–385. <https://doi.org/10.1109/JPROC.2008.2008838>.
- Yarovoy, A.G., Schukin, A.D., Kaploun, I.V., Ligthart, L.P., 2002. The Dielectric Wedge Antenna. *IEEE Trans. Antennas Propag.* 50 (10), 1460–1472.